Random singlets in the $s = 5/2$ coupled frustrated cubic lattice $Lu_3Sb_3Mn_2O_{14}$

Chanhyeon Lee,[1,*] Suheon Lee,[2,*] Heung-Sik Kim,[3] Shunichiro Kittaka,[4,5] Yoshimitsu Kohama,[5] Toshiro Sakakibara,[5] Ki Hoon Lee,[6] J. van Tol,[7] Denis I. Gorbunov,[8] Seung-Hwan Do,[9] Sungwon Yoon,[10] Adam Berlie,[11] and Kwang-Yong Choi[10,†]

[1]*Department of Physics, Chung-Ang University, Seoul 06974, Republic of Korea*
[2]*Center for Integrated Nanostructure Physics, Institute for Basic Science (IBS), Suwon 16419, Republic of Korea*
[3]*Department of Physics and Institute of Quantum Convergence Technology, Kangwon National University, Chuncheon 24311, Republic of Korea*
[4]*Department of Physics, Faculty of Science and Engineering, Chuo University, Kasuga, Bunkyo-ku, Tokyo 112-8551, Japan*
[5]*Institute for Solid State Physics, University of Tokyo, 5-1-5 Kashiwanoha, Kashiwa, Chiba 277-8581 Japan*
[6]*Department of Physics, Incheon National University, Incheon 22012, Republic of Korea*
[7]*National High Magnetic Field Laboratory, Florida State University, Tallahassee, Florida 32310-3706, USA*
[8]*Dresden High Magnetic Field Laboratory (HLD-EMFL), Helmholtz-Zentrum Dresden-Rossendorf, 01328 Dresden, Germany*
[9]*Materials Science and Technology Division, Oak Ridge National Laboratory, Oak Ridge, Tennessee 37831, USA*
[10]*Department of Physics, Sungkyunkwan University, Suwon 16419, Republic of Korea*
[11]*ISIS Neutron and Muon Source, STFC Rutherford Appleton Laboratory, Harwell Campus, Didcot, Oxfordshire OX11 0QX, United Kingdom*

(Received 19 December 2022; revised 30 March 2023; accepted 22 May 2023; published 1 June 2023)

We combine thermodynamic, electron spin resonance (ESR), and muon spin-relaxation (μSR) measurements with density functional theory (DFT) and classical Monte Carlo calculations toward understanding a disorder-driven behavior of the 3D coupled frustrated cubic lattice $Lu_3Sb_3Mn_2O_{14}$ with $s = 5/2$. The classical Monte Carlo calculations based on exchange interactions extracted from DFT predict that $Lu_3Sb_3Mn_2O_{14}$ undergoes a transition to magnetic ordering. In sharp contrast, our specific heat measurements evince a weak magnetic anomaly at 0.5 K while μSR detects neither long-range magnetic order nor spin freezing down to 0.3 K. For temperatures above 2 K, our *ac* susceptibility, magnetization, and specific heat data obey temperature-magnetic field scalings, indicative of the formation of 3D random singlets. The development of multiple ESR lines with decreasing temperature below 80 K supports the notion of inhomogeneous magnetism. Our results extend random-singlet physics to 3D frustrated classical magnets with a large spin number $s = 5/2$.

DOI: 10.1103/PhysRevB.107.214404

I. INTRODUCTION

Random singlets (RSs) offer a conceptual framework for describing the low-energy state of disordered quantum magnets. When strong quenched disorder or exchange randomness is present in spin systems, disordered quantum spin liquids (QSLs), valence-bond-glass, and random-singlet states can emerge by promoting quantum fluctuations against magnetic ordering [1–15]. The RS state comprises a random network of a minor fraction of intrinsic orphan spins and a majority of singlet dimers and resonating clusters with a broad distribution of energies. Experimental signatures of the RS state include power-law dependencies of magnetization, magnetic susceptibility, and specific heat, which emulates the low-energy power-law density of states $\rho(E) \sim E^{-\alpha}$ [10,11].

Singularly, the RS state is universal for a broad class of spin chains subject to quenched disorder and is described by an infinite-randomness fixed point (IRFP) with an infinite dynamic exponent [16,17]. In higher dimensions, it has been numerically established that the RS state possibly with a finite-randomness fixed point (FRFP) can be stabilized for various 2D and 3D frustrated magnets, such as the triangular, kagome, $J_1 - J_2$ square, and pyrochlore lattice [5–13]. Notably, a recent study of Heisenberg spin chains with competing $J_1 - J_2$ interactions revealed a phase transition from the so-called unfrustrated RS with IRFP to the frustrated RS state with increasing frustration J_2/J_1 [18]. The frustrated RS state is characterized by gapless excitations and may have a FRFP, which resembles the higher-dimensional RS states reported in frustrated 2D and 3D quantum magnets.

Experimental instances of higher-dimensional RS encompass triangular lattices $YbMgGaO_4$, $Sc_2Ga_2CuO_7$, and Y_2CuTiO_6, square lattice $Sr_2CuTe_{1-x}W_xO_6$, pyrochlore lattice $Lu_2Mo_2O_5N_2$, and Kitaev honeycomb lattices Cu_2IrO_3 and $\alpha - Ru_{1-x}Ir_xCl_3$ [19–30]. However, all RS candidate materials hitherto reported have been limited to geometrically or exchange-frustrated magnets with small spin numbers. Given that this liquid-like state contradicts the conventional wisdom that quenched randomness in magnetic insulators brings about spin freezing or spin glass, it is of paramount significance

*These authors contributed equally to this work.
†choisky99@skku.edu

to investigate whether RS physics can be extended to 3D classical frustrated magnets with a large spin number.

In this paper, we report the magnetic properties of spin-5/2 3D frustrated antiferromagnet $Lu_3Sb_3Mn_2O_{14}$, in which Mn^{2+} ($s = 5/2$) ions are arranged on a frustrated cubic lattice [31]. Our numerical calculations and specific heat show an indication that the studied compound is weakly ordered. However, the temperature and magnetic field scalings of thermodynamic data allude to the presence of RS in this classical frustrated antiferromagnet.

II. EXPERIMENTAL DETAILS

Polycrystalline samples of $Lu_3Sb_3Mn_2O_{14}$ and its nonmagnetic counterpart $Lu_3Sb_3Zn_2O_{14}$ were synthesized by the solid-state reaction method. Stoichiometric amounts of Lu_2O_3, Sb_2O_5, $MnCO_3$, and ZnO were thoroughly ground and then calcinated at 1200°C for $Lu_3Sb_3Mn_2O_{14}$ and at 1300°C for $Lu_3Sb_3Zn_2O_{14}$ for 48 h. The phase purity of the samples was examined using powder x-ray diffraction (XRD) at room temperature. We refined the XRD data using the FullProf software.

dc and *ac* magnetic susceptibilities and isothermal magnetization were measured using a VSM-SQUID (superconducting quantum interference device) magnetometer (MPMS3, Quantum Design). The *dc* magnetic susceptibility was measured in a temperature range of $T = 2 - 300$ K and in an external field of 0.1 T. Isothermal magnetization curves were recorded up to 14 T in the $T = 2 - 20$ K temperature range. *ac* susceptibility measurements were performed in a frequency range $\nu = 10 - 400$ Hz in an *ac* field of 3 Oe and zero *dc* magnetic field as well as in a field range of $\mu_0 H = 0.01 - 5$ T at a fixed frequency $\nu = 10$ Hz. High-field magnetization experiments were conducted at the Dresden High Magnetic Field Laboratory using a nondestructive pulsed magnet. An induction method with a pick-up coil was employed to detect the magnetic moment. The high-field magnetization data recorded in the $\mu_0 H = 0 - 58$ T range at $T = 2.5$ K were scaled to the isothermal magnetization obtained by SQUID in the low-field range of $\mu_0 H = 0 - 14$ T at $T = 2.5$ K.

The specific heat was measured using a standard adiabatic heat-pulse method in a dilution refrigerator (Kelvinox MX100, Oxford) with a home-built calorimeter. A magnetic field was applied using a 15-T superconducting magnet. We subtracted the addenda contribution from all presented data, which was always less than 1.5% of the sample heat capacity.

High-frequency ESR experiments were performed at $\nu = 240$ GHz with a quasioptical heterodyne spectrometer (National High Magnetic Field Laboratory in Tallahassee, Florida, USA). The temperature was varied in the $T = 2 - 200$ K range using a liquid helium cryostat. Polycrystalline samples were packed with a Teflon tube and then mounted on a small cavity. To record the ESR spectra, we swept an external magnetic field using a 12 T superconducting magnet at a fixed frequency.

For zero-field (ZF) and longitudinal-field (LF) muon spin relaxation (μSR) experiments, we exploited the ARGUS and HiFi spectrometers at the ISIS Neutron and Muon source, Rutherford Appleton Laboratory, United Kingdom. Polycrystalline samples were packed with silver foil and then mounted on the sample holder. ZF-μSR spectra were measured from $T = 2$ to 650 K with a Variox He4 cryostat and oven heater and from $T = 0.3$ to 2.5 K with a Heliox He3 cryostat. LF-μSR spectra were recorded in an external magnetic field $\mu_0 H = 0.01 - 1$ T at $T = 0.3$ (300) K using the ARGUS (HiFi) spectrometer. Because we utilized two spectrometers, ARGUS and HIFI, to cover different temperature ranges, the baseline correction for the μSR spectra was made at 300 K. The detector efficiency parameter between forward and backward detectors was determined by applying a weak transverse field of 20 G at 300 K for both spectrometers. All obtained μSR data were analyzed using the WiMDA software [32]. The μSR spectra were plotted as the muon spin polarization by normalizing the theoretically obtained asymmetry value at $t = 0$ from the fittings.

To compute magnetic exchange interactions, we first performed first-principles density functional theory (DFT) calculations using OPENMX code [33,34]. Double-zeta-single-polarization numerical atomic orbitals were used for each element as our basis set. Perdew-Burke-Ernzerhof generalized gradient approximation of the exchange-correlation functional (PBE) was employed [35] and 400 Ry of the real-space grid was adopted to solve Poisson's equation using fast-Fourier transform and to sample electrostatic potential and exchange-correlation functional. $9 \times 9 \times 9$ k-grid was used to sample the total energy. Electron correlations were treated via a simplified rotationally-invariant flavor of the DFT + U formalism, where we varied the strength of the on-site Coulomb parameter U_{eff} from 2 to 5 eV at Mn d orbitals. We computed magnetic exchange interactions using Jx code [36,37] in the presence of a Néel-type antiferromagnetic order in the entire range of U_{eff}. We confirmed the local character of Mn moments as the electronic structure of the system showed no significant difference upon enforcing ferromagnetism. The heat bath method was used for classical Monte Carlo simulations. The spin-exchange interactions were taken from the values from the DFT + U calculation with $U_{\text{eff}} = 3$ eV. The simulation has been carried out with periodic boundary conditions of $12 \times 12 \times 6$ unit cells containing 5184 spin sites. For each temperature and magnetic field, we made 30 000 measurements.

III. RESULTS AND DISCUSSION

A. Structural analysis and spin topology

Figure 1(a) presents the crystal structure of $Lu_3Sb_3Mn_2O_{14}$ ($R\bar{3}m$), where Mn^{2+} triangular layers are stacked by alternating Lu and Sb kagome layers. We recall that $Lu_3Sb_3Mn_2O_{14}$ is derived from tripod kagome materials $RE_3Mg_2Sb_3O_{14}$ (RE = rare earth) that consist of Kagome planes of magnetic rare-earth ions separated by triangular planes of nonmagnetic Mg^{2+} ions [38]. The crystal structure contains the two different crystallographic sites of Mn(1) and Mn(2): $Mn(1)O_8$ hexagonal pyramids and $Mn(2)O_6$ octahedra. All the Mn^{2+} ions are not connected to each other through corner- and edge-sharing of metal-oxygen polyhedra, and hence, magnetic interactions between Mn^{2+} ions occur via Mn-O-O-Mn super-super exchange paths.

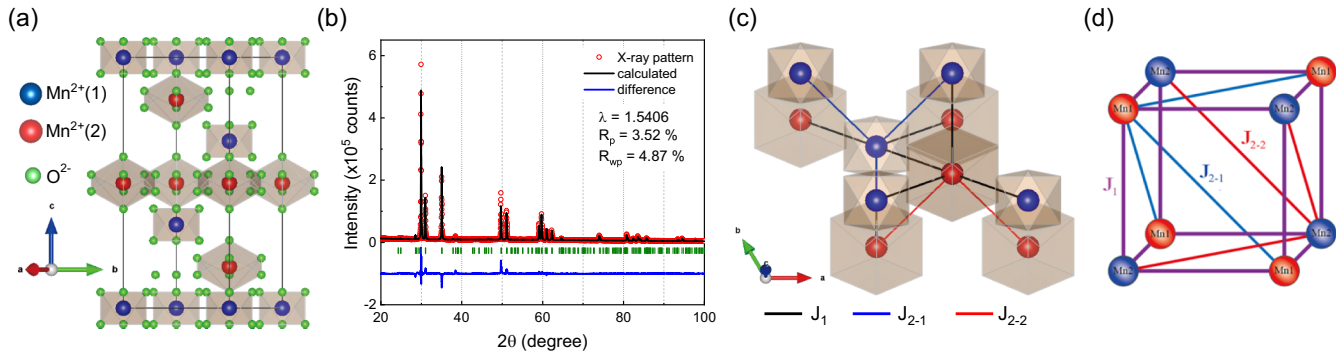

FIG. 1. (a) Crystal structure of $Lu_3Sb_3Mn_2O_{14}$ consisting of $Mn(1)O_8$ hexagonal bipyramids and $Mn(2)O_6$ octahedra. The red, blue, and green balls stand for Mn(1), Mn(2), and O atoms, respectively. The Lu and Sb atoms are omitted for clarity. (b) Rietveld refinement of the XRD powder pattern of $Lu_3Sb_3Mn_2O_{14}$. The red open circles, the solid black line, the solid blue line, and the green vertical dashes denote the experimental, calculated, difference curve, and Bragg peaks, respectively. (c) The solid lines depict the super-super exchange paths Mn-O-O-Mn, which form a three-dimensional frustrated lattice. (d) 3D frustrated cubic model composed of an edge coupling J_1 and two different face diagonal interactions J_{d1} and J_{d2}.

The powder XRD pattern of $Lu_3Sb_3Mn_2O_{14}$ measured at room temperature is shown in Fig. 1(b). The lattice parameters extracted from the Rietveld refinements are $a = 7.33243(6)$ Å, $b = 7.33243(6)$ Å, and $c = 17.2894(8)$ Å. The goodness of fit obtained by the residual refinement factors in the fitting range of $5^\circ < 2\theta < 150^\circ$ is $R_p = 3.52\%$, $R_{wp} = 4.87\%$, and $\chi^2 = 5.78$. The atomic coordinates with Wyckoff positions are summarized for $Lu_3Sb_3Mn_2O_{14}$ and its nonmagnetic counterpart in Table I. The degree of antisite mixing is less than 1%. This observation is consistent with prior findings on isostructural compounds $RE_3Sb_3Mn_2O_{14}$ (RE = La, Pr, and Nd), which show 1:3 cation ordering of Mn(1)/RE in the $3a$ site and Mn(2)/Sb in the $3b$ site due to the large difference in cation size [31].

Shown in Fig. 1(c) is the sketch of super-super exchange paths between Mn^{2+} ions. We performed DFT calculations for high-spin $3d^5$ Mn^{2+} ions to quantitatively estimate the strength of exchange interactions. Using a reasonable strength of the on-site Coulomb interaction parameter $U_{\rm eff} = 3$ eV at Mn sites, we obtain $J_1 = 1.25$ K for the nearest-neighbor Mn(1)-Mn(2) interaction [black line in Fig. 1(c)] and $J_{d1} = 0.8$ K and $J_{d2} = 0.2$ K for the next-nearest neighbor Mn(1)-Mn(1) and Mn(2)-Mn(2) interactions [blue and red lines in Fig. 1(c)], respectively. The interlayer interaction is an order of $J_{\rm inter} = 0.8$ K. The resulting spin topology is depicted in Fig. 1(d). Neglecting the interlayer interaction, the cubic lattice with J_1 running along the edges and J_{di} $(i = 1, 2)$ along the face diagonals can be first treated as a 3D Shastry-Sutherland model with $s = 5/2$ [39–41]. The Curie-Weiss (CW) temperature estimated from these calculated exchange interactions yields $\Theta_{\rm CW}^{\rm th} = -37$ K, which is in reasonable agreement with the experimental value of $\Theta_{\rm CW} = -43.48$ K [see Fig. 2(c)]. Noteworthy is that a 3D generalized Shastry-Sutherland lattice in a mean-field limit can host a valence bond crystal in addition to a Néel ordered state, depending on the relative strengths of J_1 and J_{di} [39,40]. As far as we know, however, the precise phase diagram of $s = 5/2$ 3D Shastry-Sutherland antiferromagnet with interlayer couplings is not determined. Instead, our classical Monte Carlo simulations, based on the exchange parameters derived from the DFT calculations, reveal that the studied compound lies on a magnetically ordered side [see the calculated specific heat in Fig. 4(a) below] in the absence of perturbation and quenched disorder. This is not unexpected because the face diagonal interactions J_{di} are comparable in strength to the interlayer interaction.

B. Magnetic susceptibility and magnetization

Figure 2(a) presents the T dependence of the static magnetic susceptibility $\chi(T)$ of $Lu_3Sb_3Mn_2O_{14}$ measured at $\mu_0 H = 0.1$ T in the zero-field-cooled (ZFC) and field-cooled (FC) process. No difference between the ZFC and FC $\chi(T)$ excludes the occurrence of spin freezing or spin glass. The

TABLE I. Atomic parameters of $Lu_3Sb_3Mn_2O_{14}$ and $Lu_3Sb_3Zn_2O_{14}$ obtained from the Rietveld refinement in the $R\bar{3}m$ space group.

		$Lu_3Sb_3Mn_2O_{14}$			$Lu_3Sb_3Zn_2O_{14}$		
Atom	Wyckoff site	x	y	z	x	y	z
Mn1	3a	0	0	0	0	0	0
Mn2/Zn2	3b(18g)	0	0	1/2	0	0	0360(6)
Sb	9d	1/2	0	1/2	1/2	0	1/2
Lu	9e	1/2	0	0	1/2	0	0
O1	6c	0	0	0.3956(1)	0	0	0.3968(5)
O2	18h	0.5352(2)	–0.5352(2)	0.1333(1)	0.5475(5)	–0.5475(5)	0.156(6)
O3	18h	0.1437(3)	–0.1437(3)	–0.064(0)	0.1614(5)	–0.1614(5)	–0.0405(5)

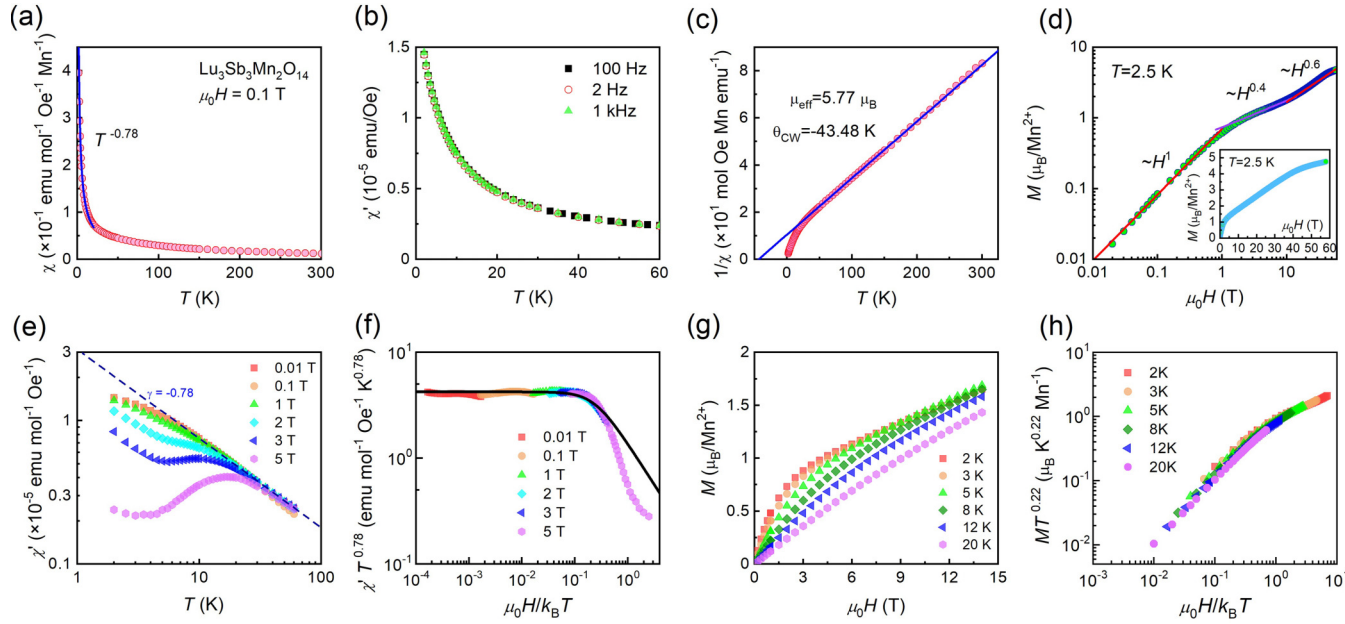

FIG. 2. (a) Temperature dependence of the dc magnetic susceptibility $\chi(T)$ of $Lu_3Sb_3Mn_2O_{14}$ in an external field of $\mu_0H = 0.1$ T. The solid blue line depicts the low-temperature power-law fit. (b) *ac* magnetic susceptibility vs temperature with three different frequency $\nu =$ 100 Hz, 200 Hz, and 1000 Hz. (c) Inverse magnetic susceptibility $1/\chi(T)$ plotted with the Curie-Weiss model fit (blue line). (d) High-field magnetization measured up to 58 T at $T = 2.5$ K on a log-log plot. The solid red lines present a power-law increase of the magnetization. The inset presents the magnetization curve in a linear scale. (e) Real component of the *ac* susceptibility $\chi'(T)$ as a function of temperature and magnetic fields measured in $\nu = 100$ Hz and an oscillating field of 10 Oe. The solid line represents a $T^{-0.78}$ dependence. (f) Scaling of $T^{0.78}\chi'$ with μ_0H/k_BT on a log-log scale. (g) Magnetization curves $M(H)$ at various temperatures. (h) Log-log scaled plot of $T^{0.22}M(H)$ with μ_0H/k_BT.

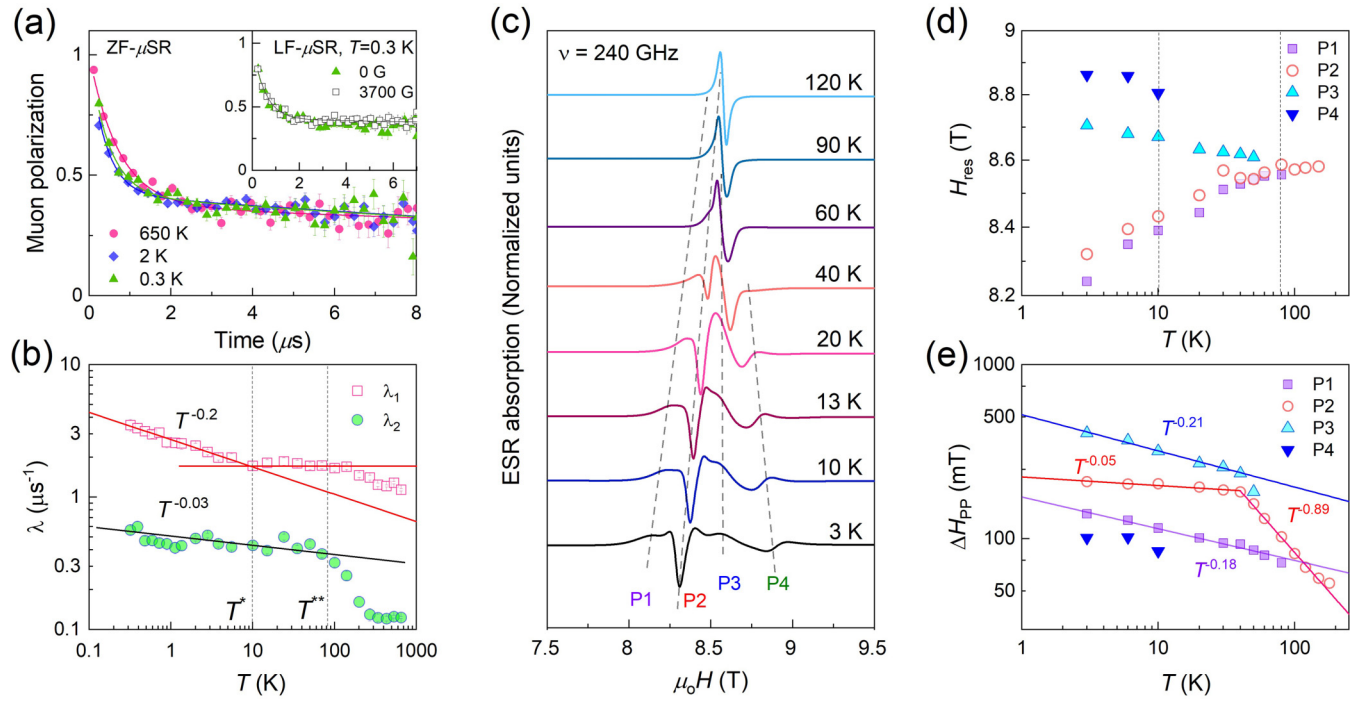

FIG. 3. (a) Time evolution of ZF-μSR spectra at selected temperatures $T = 0.3$, 2, and 650 K. The solid lines are fits as described in the main text. The inset plots the representative LF-μSR spectra taken at $T = 0.3$ K and $\mu_0H = 0$ and 0.37 T. (b) Temperature dependence of the muon spin-relaxation rates $\lambda_1(T)$ and $\lambda_2(T)$. The solid lines are fittings to the power-law behavior. (c) Thermal evolution of the high-frequency ESR spectra measured at $\nu = 240$ GHz. The dashed lines are a guide to the eye. (d) Resonance field as a function of temperature. (e) Peak-to-peak width vs temperature. The solid lines represent power-law dependencies.

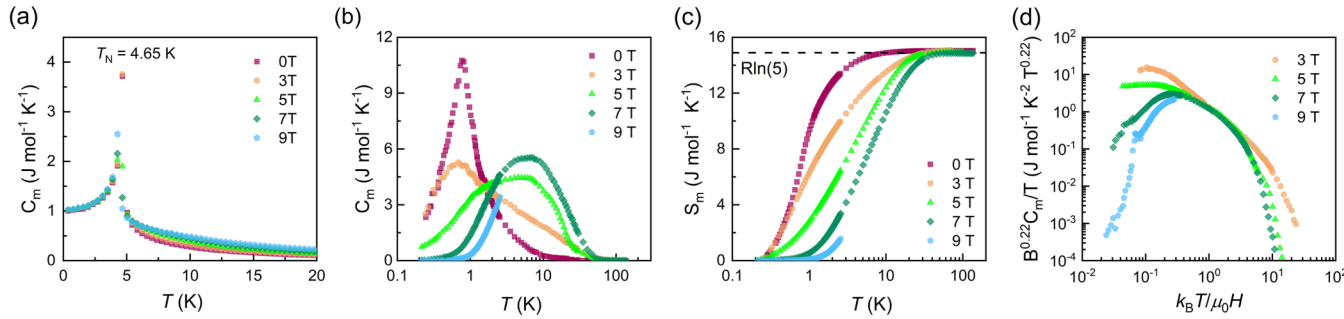

FIG. 4. (a) Temperature and field dependencies of the magnetic specific heat $C_m(T)$ calculated by classical Monte Carlo simulations. The magnetic parameters used for the simulations are determined by DFT calculations. (b) Temperature dependence of the magnetic specific heat $C_m(T)$ at selected magnetic fields $\mu_0H = 0, 3, 5, 7,$ and 9 T. $C_m(T)$ is obtained by subtracting the lattice contribution of the nonmagnetic isostructural compound $Lu_3Sb_3Zn_2O_{14}$ from the total specific heat. (c) Field and temperature dependence of the magnetic entropy $S_m(T)$. The horizontal dashed line marks the expected total entropy change Rln6 for the spin $s = 5/2$ system. (d) Scaling plot of $B^{0.22}C_m/T$ vs k_BT/μ_0H.

lacking spin-glass transition is further corroborated by the in-phase component of the ac susceptibility $\chi'(T)$, which does not show any frequency dependence, as shown in Fig. 2(b). Instead, $\chi(T)$ exhibits a power-law increase $\chi(T) \sim T^{-\alpha_s}$ ($\alpha_s \approx 0.78$) without any apparent saturation or kink for $T <$ 20 K. The CW fit of $1/\chi(T)$ in the $T = 30 - 300$ K range yields the effective magnetic moment $\mu_{\text{eff}} = 5.77\ \mu_B$ and the CW temperature $\Theta_{CW} = -43.48$ K, as shown in Fig. 2(c). The experimental μ_{eff} is close to the theoretical spin-only value of 5.82 μ_B expected for Mn^{2+} ($s = 5/2$) ions with the g factor $g = 1.97$ [determined by electron spin resonance in Fig. 3(c)]. The moderate negative Θ_{CW} suggests dominant antiferromagnetic exchange interactions between Mn^{2+} spins.

In Fig. 2(d), we show the high-field magnetization $M(H)$ measured at $T = 2.5$ K up to 58 T. With increasing field, $M(H)$ exhibits a steep rise at low fields with a subsequent linear-like increase at high fields [see the inset of Fig. 2(d)]. $M(H)$ approaches the saturation magnetization $M_S = gS\mu_B \approx 4.93\ \mu_B$ at the saturation field $\mu_0H_S \approx 45$ T, which is comparable to $\Theta_{CW} = -43.48$ K. The low-field increase in $M(H)$, resembling the Brillouin function, indicates the presence of orphan-like or weakly correlated spins, which constitute 16% of the total Mn^{2+} spins. Since our XRD reveals that $Lu_3Sb_3Mn_2O_{14}$ contains a small amount of anti-site disorder, Mn^{2+} vacancies and defects can give rise to both intrinsic orphan spins in the RS state and paramagnetic free spins in the non-RS state, which are hardly distinguishable in the static magnetization [42]. As depicted in Fig. 1(d), the Mn(1)/Mn(2) defects randomize the J_{d1} and J_{d2} interactions. To inspect the influence of exchange randomness and spin vacancies on the magnetization behavior, we plot $M(H)$ on a log-log scale, enabling the identification of its three-stage increase. Specifically, the magnetization follows a power-law-like increase, $M(H) \propto H^{1-\alpha_m}$ with the exponent $\alpha_m \approx 0$ in a field range of $\mu_0H = 0 - 1$ T, $\alpha_m \approx 0.6$ at $\mu_0H = 1 - 10$ T, and $\alpha_m \approx 0.4$ at $\mu_0H = 10 - 40$ T. For magnetic fields above 1 T, the power-law $M(H)$ with the exponent $0 < \alpha_m < 1$ indicates random magnetism. The extracted exponent is somewhat smaller than $\alpha_s \approx 0.78$ deduced from $\chi(T)$.

Exhibited in Fig. 2(e) are the H and T dependencies of $\chi'(H, T)$ measured at a fixed frequency $\nu = 100$ Hz in various dc fields of $\mu_0H = 0.01 - 5$ T. With increasing field, $\chi'(H, T < 30\ \text{K})$ is systematically reduced, the freezing out of weakly coupled spins under an external magnetic field. Consequently, we are able to single out the broad $T = 20$ K maximum feature for $\chi'(\mu_0H = 5\ \text{T}, T)$, concealed by the sub-Curie increase in the low-field data. In Fig. 2(f), we showcase the scaling behavior by plotting $T^{\alpha}\chi'$ vs μ_0H/k_BT. Remarkably, the data fall onto a single curve (solid line) with $\alpha_s = 0.78$ over three orders of magnitude. Further supportive evidence for the scaling relation is provided by the H and T dependencies of $M(H, T)$ measured up to $\mu_0H = 14$ T at various temperatures $T = 2 - 20$ K [see Fig. 2(g)]. By plotting $T^{\alpha_s-1}M(H)$ against μ_0H/k_BT in Fig. 2(h), we demonstrate the data collapse with the scaling exponent $\alpha_s \approx 0.78$ over three orders of magnitude. Taken together, the commonly observed scaling relations of $\chi'(H, T)$ and $M(H, T)$ with the complimentary exponent indicate that the studied system hosts random singlets and bond-disordered spin states, as reported in other frustrated magnets subject to quenched disorder.

C. Muon spin-relaxation and electron spin resonance

To shed light on the ground-state spin dynamics, we turn to local dynamical probes of spin fluctuations. In Fig. 3(a), we exhibit presentative ZF-μSR spectra, which show little variation with temperature. The lack of an oscillatory signal down to 0.3 K alludes to the absence of long-range magnetic order. The μSR spectra are well described by the sum of two simple exponential functions $P_z(t) = f\exp(-\lambda_1 t) + (1 - f)\exp(-\lambda_2 t)$, where λ_1 (λ_2) is the fast (slow) muon spin relaxation rate and f is the fraction of the fast-relaxing component. As the temperature decreases to 0.3 K, the fraction of the fast-relaxing component increases monotonically from $f \sim 0.55$ to 0.78, indicative of a gradual slowing down of spin correlations. The two components may be related to two different magnetic environments, alluding to the presence of inhomogeneous magnetic states. The exponentially decaying relaxation function implies that the dynamical field is of electronic origin. This is further supported by the observation that the muon spin polarization is hardly recovered by the applied longitudinal field [see the inset of Fig. 3(a)].

In Fig. 3(b), we plot the muon spin-relaxation rates $\lambda_1(T)$ and $\lambda_2(T)$ as a function of temperature. On cooling from 650 K, the fast relaxation component $\lambda_1(T)$ increases

gradually, and then flattens off below 80 K, and finally shows a power-law increase $\lambda_1(T) \sim T^{-0.2}$ in the temperature range of 0.3 K $< T <$ 10 K. On the other hand, the slow relaxation rate $\lambda_2(T)$ displays a steep increase through 100 K and varies slowly with a power-law dependence $\lambda_2(T) \sim T^{-0.03}$ below 80 K. We can identify two crossover temperatures at $T^* =$ 10 K and $T^{**} = 80$ K, where spin dynamics shows a marked change. In the inset of Fig. 3(a), we plot the LF-μSR spectra measured at $T = 0.3$ K. Remarkably, we do not observe any decoupling behavior under the 1 T LF, even at $T = 300$ K (not shown here). Considering the magnetic energy scale of $\Theta_{CW} = -43.48$ K, the LF-μSR results suggest the presence of additional relaxation channels, requiring further investigation for clarification. Taken together, the combined ZF- and LF-μSR data indicate the presence of two distinct dynamically fluctuating states that govern the spin dynamics of the 3D $s = 5/2$ frustrated magnet $Lu_3Sb_3Mn_2O_{14}$. As the fraction of the fast relaxation component grows with lowering temperature, $\lambda_1(T)$ pertains to the thermal evolution of a RS-like state, while $\lambda_2(T)$ is associated with the development of a weakly correlated state.

We turn to high-frequency ESR. As shown in Fig. 3(c), the ESR signal consists of a single Lorentzian profile in the high-T paramagnetic state. On cooling down through $T^{**} = 80$ K, two secondary signals are split off from the primary signal. Eventually, one more ESR signal appears below $T^* = 10$ K. We stress that both μSR and ESR feature anomalies at the two characteristic temperatures. Since the secondary signals shift to higher or lower fields, the newly emerging ESR lines cannot be attributed to simple defects or orphan spins. Rather, they may be related to the development of distinct correlated magnetic states due the combination of frustrated spin topology and spin vacancies. All the ESR spectra are fitted to a sum of four powder-averaged Lorentzian profiles for quantitative analysis of the ESR parameters. The extracted resonance field H_{res} and the peak-to-peak linewidth ΔH_{pp} are plotted in Figs. 3(d) and 3(e). As the temperature is lowered from 80 K, $H_{res}(T)$s of the P1 and P2 absorption lines shift to lower fields, while those of the P3 and P4 lines increase towards higher fields. Given that H_{res} is proportional to internal magnetic fields, this trend implies that some spins develop ferromagnetic correlations, while others develop antiferromagnetic correlations. In the temperature range of $T =$ 3 − 120 K, $\Delta H_{pp}(T)$ follows a critical power law $\Delta H_{pp} \propto T^{-\alpha}$ with the exponents of $\alpha = 0.18$ for P1 and 0.21 for P3. Besides, we observe a changing exponent from $\alpha = 0.89$ to 0.05 through 40 K. The critical-like line broadening at low temperatures may be due to the development of local spin correlations or spatially random local fields. We recall that a triangular antiferromagnet $Ba_3CuSb_2O_9$ with Cu^{2+}/Sb^{5+} disorders shows the critical ESR line broadening that is taken as a sign of a random singlet state [43]. As such, our ESR results witness the presence of inhomogeneous magnetic states.

D. Magnetic specific heat and its scaling

We further address the nature of low-lying magnetic excitations. Figure 4(a) presents the calculated magnetic specific heat $C_m(T, H)$ based on classical Monte Carlo simulations. The magnetic parameters used for the simulations were obtained by DFT calculations. The theoretical $C_m(T, H)$ shows magnetic ordering at $T_N = 4.65$ K in zero field. With increasing field of up to $\mu_0 H = 9$ T, the transition temperature is slightly reduced. In Fig. 4(b), we plot the experimental magnetic specific heat C_m as a function of temperature under external magnetic fields of $\mu_0 H = 0 - 9$ T (the incomplete 9 T data due to technical issues). The specific heat of a nonmagnetic analog $Lu_3Sb_3Zn_2O_{14}$ was used to subtract a lattice contribution from the total specific heat. In addition, the nuclear Schottky anomaly seen in high fields is also subtracted to extract $C_m(T)$ (not shown here). The zero-field $C_m(T)$ data exhibit a maximum at $T = 0.5$ K. On the application of an external magnetic field, the maximum is rapidly suppressed, which is rapidly suppressed on the application of an external magnetic field. This suggests that a minor fraction of spins is frozen, although this weak magnetic anomaly is hidden to μSR [see Fig. 3(a)]. In contrast, the higher-T broad hump feature becomes enhanced. The broad hump shifts toward higher temperatures with increasing field, reminiscent of orphan-like spins. The $T = 7$ K hump of $C_m(T)$ at $\mu_0 H = 5 - 9$ T is correlated with the $T = 20$ K maximum of $\chi'(\mu_0 H = 5$ T), which is typical for short-range magnetic order. Overall, we find a noticeable discrepancy between the theoretical and experimental $C_m(T, H)$. The experimental specific heat reflects the low-energy landscape modified by quenched disorder, as evidenced by the appearance of inhomogeneous magnetism in the ESR data.

The magnetic entropy $S_m(T, H)$, calculated by integrating C_m/T, is shown in Fig. 4(c). $S_m(T, H)$ reaches the theoretically expected value $R \ln(2s + 1) = 15.44$ JK^{-2}/(mol Mn) for $s = 5/2$ as the temperature is raised to $T = |\Theta_{CW}|(=$ 43.48 K). At zero field, the majority of $S_m(T, H)$ is released below $T = 10$ K. With increasing field, the low-T $S_m(T, H)$ is systematically reduced, while the onset temperature of the entropy release shifts towards the temperature scale of Θ_{CW}. This indicates a massive pile-up of the low-energy density of states, which consist of weakly coupled spins and thus are quickly suppressed by applying an external field. Lastly, we examine the scaling relation of the $C_m(T, H)$ data, $(\mu_0 H)^\gamma C_m/T = F(k_B T/\mu_0 H)$ with a scaling function F. Unlike $\chi'(H, T)$ and $M(H, T)$, we find data collapse only in a limited range with $\gamma = 0.22$, invalidating the extracted exponent. This incomplete scaling of $C_m(T, H)$ is not surprising, given that $C_m(T, H)$ features two energy scales and Mn vacancies. As shown in Fig. 1(d), the Mn(1)/Mn(2) defects or vacancies introduce randomness in J_{d1} and $J_{d1}(\neq J_{d2})$ exchange interactions, while preserving $J_1 - J_{d1}$ (or $J_1 - J_{d2}$) frustration. Considering that the clean $Lu_3Sb_3Mn_2O_{14}$ compound is situated close to a valence bond solid (VBS) from a Néel ordered state, a disorder-driven emergent spin lattice could lead to a broken VBS in favor of a RS state over a spin glass [44].

IV. CONCLUSIONS

We have performed thermodynamic and local resonance measurements of $Lu_3Sb_3Mn_2O_{14}$ supplemented with DFT and classical Monte Carlo calculations. Our theoretical modeling unravels that $Lu_3Sb_3Mn_2O_{14}$ is best described as a 3D Shastry-Sutherland antiferromagnet with interlayer

couplings. In the absence of disorder, $Lu_3Sb_3Mn_2O_{14}$ is calculated to undergo a magnetic transition at $T_N = 4.65$ K. Contrarily, our specific heat data show a magnetic anomaly at $T = 0.5$ K, hidden to μSR. The absence of longitudinal field-decoupling confirms the dynamic nature of spin fluctuations probed by μSR. Quenched disorder turns out to drive the studied system to an inhomogeneous magnetic state made of random singlets and a small fraction of frozen spins.

Further, our μSR and ESR data uncover two crossover temperatures at $T^* = 10$ K and $T^{**} = 80$ K, where spin correlations develop a distinct thermal variation. The concurring shift of the ESR resonance field and the power-law increase of the ESR linewidth, together with the weak power-law increase of the muon spin-relaxation rate, advocate the development of inhomogeneous, correlated magnetic states. Notably, we identify scaling collapses of the magnetic-field- and temperature-dependent $\chi'(H, T)$ and $M(H, T)$ as expected from random singlet physics. The common exponent extracted from the power-law behaviors suggests the presence of the low-energy power-law density of states $\rho(E) \sim E^{-\alpha_s}$ ($\alpha_s = 0.78$). However, the incomplete $C_m(T, H)$ scaling signifies an inhomogeneous magnetic state.

In $Lu_3Sb_3Mn_2O_{14}$, where quantum fluctuations are suppressed, the quenched disorder is apt to induce spin glass. In sharp contrast to conventional wisdom, the observed random singlet demonstrates that strong disorder can stabilize a random-singlet state even in a classical frustrated cubic antiferromagnet. The proximity to spin dimers might be a prerequisite for achieving random singlets, calling for future theoretical investigations.

ACKNOWLEDGMENTS

The work at CAU and SKKU was supported by the National Research Foundation (NRF) of Korea (Grants No. 2020R1A2C3012367, No. 2020R1A5A1016518, and No. 2019R1A2C1085907). H.-S.K. acknowledges the support of the NRF Korea (Grant No. 2020R1C1C1005900), and also the support of computational resources including technical assistance from the National Supercomputing Center of Korea (Grant No. KSC-2021-CRE-0222). The National High Magnetic Field Laboratory is supported by the National Science Foundation through Grant No. NSF/DMR-1644779 and the State of Florida. We further acknowledge the support of HLD at HZDR, member of the European Magnetic Field Laboratory (EMFL).

[1] O. Motrunich, S.-C. Mau, D. A. Huse, and D. S. Fisher, Infinite randomness quantum Ising critical fixed points, Phys. Rev. B **61**, 1160 (2000).

[2] J. Oitmaa and O. P. Sushkov, Two-Dimensional Randomly Frustrated Spin-1/2 Heisenberg Model, Phys. Rev. Lett. **87**, 167206 (2001).

[3] Y.-C. Lin, H. Rieger, N. Laflorencie, and F. Iglói, Strong-disorder renormalization group study of $S = 1/2$ Heisenberg antiferromagnet layers and bilayers with bond randomness, site dilution, and dimer dilution, Phys. Rev. B **74**, 024427 (2006).

[4] R. R. P. Singh, Valence Bond Glass Phase in Dilute Kagome Antiferromagnets, Phys. Rev. Lett. **104**, 177203 (2010).

[5] K. Watanabe, H. Kawamura, H. Nakano, and T. Sakai, Quantum spin-liquid behavior in the spin-1/2 random Heisenberg antiferromagnet on the triangular lattice, J. Phys. Soc. Jpn. **83**, 034714 (2014).

[6] H. Kawamura, K. Watanabe, and T. Shimokawa, Quantum spin-liquid behavior in the spin-1/2 random-bond Heisenberg antiferromagnet on the kagome lattice, J. Phys. Soc. Jpn. **83**, 103704 (2014).

[7] T. Shimokawa, K. Watanabe, and H. Kawamura, Static and dynamical spin correlations of the S=1/2 random-bond antiferromagnetic Heisenberg model on the triangular and kagome lattices, Phys. Rev. B **92**, 134407 (2015).

[8] L. Liu, H. Shao, Y.-C. Lin, W. Guo, and A. W. Sandvik, Random-Singlet Phase in Disordered Two-Dimensional Quantum Magnets, Phys. Rev. X **8**, 041040 (2018).

[9] K. Uematsu and H. Kawamura, Randomness-induced quantum spin liquid behavior in the $s = 1/2$ random J1-J2 Heisenberg antiferromagnet on the square lattice, Phys. Rev. B **98**, 134427 (2018).

[10] I. Kimchi, J. P. Sheckelton, T. M. McQueen, and P. A. Lee, Scaling and data collapse from local moments in frustrated disordered quantum spin systems, Nat. Commun. **9**, 4367 (2018).

[11] I. Kimchi, A. Nahum, and T. Senthil, Valence Bonds in Random Quantum Magnets: Theory and Application to $YbMgGaO_4$, Phys. Rev. X **8**, 031028 (2018).

[12] H.-Q. Wu, S.-S. Gong, and D. N. Sheng, Randomness-induced spin-liquid-like phase in the spin-1/2 J1-J2 triangular Heisenberg model, Phys. Rev. B **99**, 085141 (2019).

[13] K. Uematsu, and H. Kawamura, Randomness-Induced Quantum Spin Liquid Behavior in the $s = 1/2$ Random-Bond Heisenberg Antiferromagnet on the Pyrochlore Lattice, Phys. Rev. Lett. **123**, 087201 (2019).

[14] H. Kawamura and K. Uematsu, Nature of the randomness-induced quantum spin liquids in two dimensions, J. Phys.: Condens. Matter **31**, 504003 (2019).

[15] L. Liu, W. Guo, and A. W. Sandvik, Quantum-critical scaling properties of the two-dimensional random-singlet state, Phys. Rev. B **102**, 054443 (2020).

[16] S-k. Ma, C. Dasgupta, and C.-k. Hu, Random Antiferromagnetic Chain, Phys. Rev. Lett. **43**, 1434 (1979).

[17] D. S. Fisher, Random antiferromagnetic quantum spin chains, Phys. Rev. B **50**, 3799 (1994).

[18] K. Uematsu, T. Hikihara, and H. Kawamura, Frustration-induced quantum spin liquid behavior in the $s = 1/2$ random-bond Heisenberg antiferromagnet on the zigzag chain, J. Phys. Soc. Jpn. **90**, 124703 (2021).

[19] P. Khuntia, R. Kumar, A. V. Mahajan, M. Baenitz, and Y. Furukawa, Spin liquid state in the disordered triangular lattice $Sc_2Ga_2CuO_7$ revealed by NMR, Phys. Rev. B **93**, 140408(R) (2016).

[20] Z. Zhu, P. A. Maksimov, S. R. White, and A. L. Chernyshev, Disorder-Induced Mimicry of a Spin Liquid in $YbMgGaO_4$, Phys. Rev. Lett. **119**, 157201 (2017).

[21] W. Hong, L. Liu, C. Liu, X. Ma, A. Koda, X. Li, J. Song, W. Yang, J. Yang, P. Cheng, H. Zhang, W. Bao, X. Ma, D. Chen, K. Sun, W. Guo, H. Luo, A. W. Sandvik, and S. Li, Extreme

Suppression of Antiferromagnetic Order and Critical Scaling in a Two-Dimensional Random Quantum Magnet, Phys. Rev. Lett. **126**, 037201 (2021).

[22] O. Mustonen, S. Vasala, E. Sadrollahi, K. P. Schmidt, C. Baines, H. C. Walker, I. Terasaki, F. J. Litterst, E. Baggio-Saitovitch, and M. Karppinen, Spin-liquid-like state in a spin-1/2 square-lattice antiferromagnet perovskite induced by $d10$–$d0$ cation mixing, Nat. Commun. **9**, 1085 (2016).

[23] O. Mustonen, S. Vasala, K. P. Schmidt, E. Sadrollahi, H. C. Walker, I. Terasaki, F. J. Litterst, E. Baggio-Saitovitch, and M. Karppinen, Tuning the $S = 1/2$ square-lattice antiferromagnet $Sr_2Cu(Te_{1-x}W_x)O_6$ from Néel order to quantum disorder to columnar order, Phys. Rev. B **98**, 064411 (2018).

[24] S. Yoon, W. Lee, S. Lee, J. Park, C. H. Lee, Y. S. Choi, S.-H. Do, W.-J. Choi, W.-T. Chen, F. Chou, D. I. Gorbunov, Y. Oshima, A. Ali, Y. Singh, A. Berlie, I. Watanabe, and K.-Y. Choi, Quantum disordered state in the J1-J2 square-lattice antiferromagnet $Sr_2Cu(Te_{0.95}W_{0.05})O_6$, Phys. Rev. Mater. **5**, 014411 (2021).

[25] L. Clark, G. J. Nilsen, E. Kermarrec, G. Ehlers, K. S. Knight, A. Harrison, J. P. Attfield, and B. D. Gaulin, From Spin Glass to Quantum Spin Liquid Ground States in Molybdate Pyrochlores, Phys. Rev. Lett. **113**, 117201 (2014).

[26] S. K. Dey, K. Ishida, H. Okabe, M. Hiraishi, A. Koda, T. Honda, J. Yamaura, H. Kageyama, and R. Kadono, Local spin dynamics in the geometrically frustrated Mo pyrochlore antiferromagnet $Lu_2Mo_2O_{5-y}N_2$, Phys. Rev. B **107**, 024407 (2023).

[27] Y. S. Choi, C. H. Lee, S. Lee, S. Yoon, W.-J. Lee, J. Park, A. Ali, Y. Singh, J.-C. Orain, G. Kim, J.-S. Rhyee, W.-T. Chen, F. Chou, and K.-Y. Choi, Exotic Low-Energy Excitations Emergent in the Random Kitaev Magnet Cu_2IrO_3, Phys. Rev. Lett. **122**, 167202 (2019).

[28] S.-H. Do, C. H. Lee, T. Kihara, Y. S. Choi, S. Yoon, K. Kim, H. Cheong, W.-T. Chen, F. Chou, H. Nojiri, and K.-Y. Choi, Randomly Hopping Majorana Fermions in the Diluted Kitaev System $\alpha - Ru_{0.8}Ir_{0.2}Cl_3$, Phys. Rev. Lett. **124**, 047204 (2020).

[29] S.-H. Baek, H. W. Yeo, S.-H. Do, K.-Y. Choi, L. Janssen, M. Vojta, and B. Büchner, Observation of a random singlet state in a diluted Kitaev honeycomb material, Phys. Rev. B **102**, 094407 (2020).

[30] K. Kataoka, D. Wulferding, T. Yajima, D. Nishio-Hamane, D. Hirai, S. Y. Lee, K.-Y. Choi, and Z. Hiroi, Dimer crystallization induced by elemental substitution in the honeycomb lattice of $Ru_{1-x}Os_xCl_3$, J. Phys. Soc. Jpn. **91**, 014801 (2022).

[31] W. T. Fu and D. J. W. IJdo, Crystal structure of $Mn_2Ln_3Sb_3O_{14}$ (*Ln*=La, Pr and Nd): A new ordered rhombohedral pyrochlore, J. Solid State Chem. **213**, 165 (2014).

[32] F. L. Pratt, WIMDA: A muon data analysis program for the Windows PC, Phys. B: Condens. Matter **289-290**, 710 (2000).

[33] T. Ozaki, Variationally optimized atomic orbitals for large-scale electronic structures, Phys. Rev. B **67**, 155108 (2003).

[34] T. Ozaki, and H. Kino, Numerical atomic basis orbitals from H to Kr, Phys. Rev. B **69**, 195113 (2004).

[35] J. P. Perdew, K. Burke, and M. Ernzerhof, Generalized Gradient Approximation Made Simple, Phys. Rev. Lett. **77**, 3865 (1996).

[36] S. L. Dudarev, G. A. Botton, S. Y. Savrasov, C. J. Humphreys, and A. P. Sutton, Electron-energy-loss spectra and the structural stability of nickel oxide: An LSDA+U study, Phys. Rev. B **57**, 1505 (1998).

[37] H. Yoon, T. J. Kim, J.-H. Sim, and M. J. Han, Jx: An open-source software for calculating magnetic interactions based on magnetic force theory, Comput. Phys. Commun. **247**, 106927 (2020).

[38] J. A. M. Paddison, H. S. Ong, J. O. Hamp, P. Mukherjee, X. Bai, M. G. Tucker, N. P. Butch, C. Castelnovo, M. Mourigal, and S. E. Dutton, Emergent order in the kagome Ising magnet $Dy_3Mg_2Sb_3O_{14}$, Nat. Commun. **7**, 13842 (2016).

[39] D. Carpentier and L. Balents, Field theory for generalized Shastry-Sutherland models, Phys. Rev. B **65**, 024427 (2001).

[40] N. Surendran and R. Shankar, Generalized Shastry-Sutherland models in three and higher dimensions, Phys. Rev. B **66**, 024415 (2002).

[41] A. Grechnev, Exact ground state of the Shastry-Sutherland lattice with classical Heisenberg spins, Phys. Rev. B **87**, 144419 (2013).

[42] M. B. Sanders, The synthesis and characterization of novel 2D rare earth oxides for the study of frustrated magnetism, Ph.D. thesis, Princeton University, 2017.

[43] S.-H. Do, J. van Tol, H. D. Zhou, and K.-Y. Choi, Dynamical spin-orbital correlations versus random singlets in $Ba_3CuSb_2O_9$ investigated by magnetization and electron spin resonance, Phys. Rev. B **90**, 104426 (2014).

[44] Y. Imry and S. K. Ma, Random-Field Instability of the Ordered State of Continuous Symmetry, Phys. Rev. Lett. **35**, 1399 (1975).